



PERGAMON

Journal of the Mechanics and Physics of Solids
51 (2003) 1347–1369

JOURNAL OF THE
MECHANICS AND
PHYSICS OF SOLIDS

www.elsevier.com/locate/jmps

On the fracture toughness of ferroelastic materials

Chad M. Landis*

*Department of Mechanical Engineering and Materials Science, MS 321, Rice University,
P.O. Box 1892, Houston, TX 772511892, USA*

Received 31 January 2003; received in revised form 6 April 2003; accepted 7 April 2003

Abstract

The toughness enhancement due to domain switching near a steadily growing crack in a ferroelastic material is analyzed. The constitutive response of the material is taken to be characteristic of a polycrystalline sample assembled from randomly oriented tetragonal single crystal grains. The constitutive law accounts for the strain saturation, asymmetry in tension versus compression, Bauschinger effects, reverse switching, and strain reorientation that can occur in these materials due to the non-proportional loading that arises near a propagating crack. Crack growth is assumed to proceed at a critical level of the crack tip energy release rate. Detailed finite element calculations are carried out to determine the stress and strain fields near the growing tip, and the ratio of the far field applied energy release rate to the crack tip energy release rate. The results of the finite element calculations are then compared to analytical models that assume the linear isotropic K-field solution holds for either the near tip stress or strain field. Ultimately, the model is able to account for the experimentally observed toughness enhancement in ferroelastic ceramics.

© 2003 Elsevier Science Ltd. All rights reserved.

Keywords: A. Fracture toughness; Twinning; B. Crack mechanics; Ferroelectric material; C. Finite elements

1. Introduction

Ferroelectric ceramics are used in applications ranging from actuators and sensors to ultrasonic motors. A significant shortcoming of these materials in structural applications is their inherent brittleness. Specifically, most ferroelectrics have fracture toughness levels on the order of $K_{Ic} = 1 \text{ MPa}\sqrt{\text{m}}$. A characteristic of ferroelectric ceramics that

* Tel.: +1-7133483609; fax: +1-7133485423.

E-mail address: landis@rice.edu (C.M. Landis).

makes them useful as smart materials is their ability to deform and change polarization irreversibly by the mechanism of domain switching. In a manner akin to transformation toughening, domain switching leads to R-curve behavior and toughness enhancement during crack growth in ferroelectrics. Hence, an understanding of the dissipation due to domain switching and the fracture mechanics governing these materials is crucial for the efficient design of ferroelectric devices.

As an initial investigation, this paper will focus on fracture in unpoled ferroelectric ceramics under mechanical loading. Note that in the absence of electrical loading, unpoled ferroelectrics remain unpoled. Hence, unpoled ferroelectrics loaded mechanically exhibit purely ferroelastic response; i.e. irreversible straining as a result of applied stress. Experimental investigations on unpoled ferroelectric ceramics by Meschke et al. (2000), Lucato et al. (2000) and Oates et al. (2003) have found toughness enhancements in the range of $\Delta K_{Ic} = 40\text{--}100\%$ of the initiation toughness, which corresponds to $\Delta G_c = 100\text{--}300\%$. Here ΔK_{Ic} represents the difference in the steady state and initiation levels of fracture toughness during crack propagation. Generally, this toughness enhancement has been attributed to ferroelastic domain switching near the crack tip.

A number of theoretical investigations of switch toughening have been carried out (Zhu and Yang, 1997; Yang and Zhu, 1998; Reece and Guiu, 2002; Kreher, 2002) that follow the approximate methods used to analyze transformation toughening developed by McMeeking and Evans (1982) and Budiansky et al. (1983). With the exception of the work of Kreher (2002), the models applied above assume that domain switching near the crack tip occurs as a discrete transformation. More specifically, for the case of pure ferroelasticity, switching is assumed to occur at a well-defined level of stress. Once this level of stress is achieved the material accumulates a finite pre-determined level of irreversible strain. The switch is all or none, and there is no partial transformation allowed. Finally, once the switch occurs the irreversible strain cannot be reverse-switched or reoriented; it is locked into the material. This is an approximation to the actual ferroelastic constitutive behavior. In reality, switching takes place over a range of stress levels, transformation is limited by kinematic and equilibrium constraints, and strain reorientation can occur. The previously stated approximations have been used for at least two reasons. First, for most switching criteria the transformation toughening models can be solved analytically. Second, until very recently, no multi-axial incremental constitutive law for ferroelastic switching has been available to analyze this problem.

In this work, the newly developed constitutive law of Landis (2003) for ferroelastic switching is applied to the ferroelastic cracking problem. Some characteristics of the ferroelastic behavior of ferroelectric ceramics include asymmetry in the levels of attainable irreversible strain in tension versus compression, Fett et al. (1998) and Fett and Thun (1998), a Bauschinger effect upon reverse loading, and reorientation of the irreversible strain with reorientation of the applied stress. Due to the non-proportional loading experienced by material elements near a passing crack tip, the effects of unloading and strain reorientation are significant in the determination of the quantitative effects of domain switching on the toughness of ferroelastic materials. The constitutive law to be used here is cast in incremental form and captures all of the features described above.

The remainder of the paper is organized as follows. Section 2 presents the constitutive law used to describe polycrystalline ferroelastic materials. Section 3 presents the fracture model and the finite element method implemented to determine the fields near a steadily growing crack and the crack tip energy release rate. Results for the toughness enhancement predicted by the model will also be presented in this section. Section 4 will present two types of approximate models for the toughness enhancement: semi-analytical and analytical. The two types of semi-analytical models will apply the steady-state version of the J -integral, the constitutive law of Section 2 and the assumption that either the stresses or strains are given by the elastic asymptotic K-field to approximate the toughness enhancement. Then, two analytical discrete switching models will be presented for comparison to the predictions of the model in Section 3. Finally, Section 5 will be used to discuss the results and their comparison to experimental observations.

2. Constitutive law for ferroelastic switching

The non-linear constitutive response of ferroelastic ceramics is a result of the mechanism of domain switching. The crystal structure of many ferroelectrics of technological interest is tetragonal, and single crystals of ferroelectric material are divided into domains where each domain has a single crystallographic variant. In other words, within a single domain the orientation of the c -axis of the unit cells is identical. Within a single crystal, domains of different variants are separated by domain walls, and domain switching proceeds in an incremental fashion by the motion of these walls. Since the volume of the variants on either side of a domain wall is identical, domain switching can only result in irreversible *shear* strains. Note here that we are concerned with ferroelasticity and hence 90° switching only, since 180° switching does not lead to irreversible strains. A more detailed discussion of domain switching and the constitutive behavior of single crystals can be found in Huber et al. (1999), Kamlah (2001), or Landis (2003). Here we are interested in the behavior of ferroelastic *polycrystals* and a phenomenological constitutive description that can be readily implemented within finite element computations.

In order to maintain simplicity, isotropic elastic response and linear kinematics will be assumed such that the stress–strain relations can be written as

$$\varepsilon_{ij} = \frac{1 + \nu}{E} \sigma_{ij} - \frac{\nu}{E} \sigma_{kk} \delta_{ij} + \varepsilon_{ij}^r. \quad (2.1)$$

Here, ε_{ij} and σ_{ij} are the Cartesian components of the infinitesimal strain tensor and Cauchy stress tensor, ν is the Poisson's ratio and E is the Young's modulus. Also, ε_{ij}^r are the Cartesian components of the remanent strain tensor. The remanent strain is the irreversible strain and can also be referred to as the plastic strain. In all cases discussed in this paper, the datum for remanent strain corresponds to the state of the material as cooled from above the Curie temperature. In this reference state, all possible domain orientations are equally likely.

The purpose of the non-linear constitutive law is to provide the evolution of the remanent strain history given the stress or total strain history. Consistent with the facts

that domain switching gives rise to only deviatoric strains and ferroelastic ceramics exhibit kinematic hardening effects, it is assumed that the material responds elastically within a switching (yield) surface Φ described by

$$\Phi = \frac{3}{2}(s_{ij} - s_{ij}^B)(s_{ij} - s_{ij}^B) - \sigma_0^2 = 0. \quad (2.2)$$

If the stress state is on the switching surface and the load increment induces remanent straining, then the remanent strain increment is normal to the switching surface such that

$$\varepsilon_{ij}^r = \lambda(s_{ij} - s_{ij}^B). \quad (2.3)$$

Here s_{ij} are the components of the stress deviator such that $s_{ij} = \sigma_{ij} - \delta_{ij}\sigma_{kk}/3$, s_{ij}^B are the components of the deviator of the back stress tensor σ_{ij}^B , σ_0 is the initial switching (yield) strength of the material in tension or compression, and λ is the as yet undetermined plastic multiplier.

The back stress tensor leads to kinematic hardening and must be used to enforce the remanent strain saturation conditions. The approach used to determine the back stresses is based on the assumption that the internal state of the ferroelastic material is completely characterized by the components of the remanent strain tensor, Cocks and McMeeking (1999) and Landis (2002a). This assumption leads to the identification of a remanent potential, $\Psi^r(\varepsilon_{ij}^r)$, such that the back stresses are derived from the potential in the following manner:

$$\sigma_{ij}^B = \frac{\partial \Psi^r}{\partial \varepsilon_{ij}^r}. \quad (2.4)$$

In order to complete the constitutive theory, the form of Ψ^r must be specified. As previously noted, ferroelectric ceramics exhibit an asymmetry in the attainable levels of remanent strain in tension versus compression. Specifically, micromechanical simulations by Frölich (2001) and Landis (2003) suggest that the ratio of remanent strain possible in tension to that possible in compression is 1.37:1. Furthermore, this theoretical value is in the same range as the ratio of the maximum poling remanent strain to the maximum compressive remanent strain due to stress depolarization measured in PLZT by Lynch (1996), and in PZT by Fang and Li (1999). Unfortunately, knowledge of the saturation strains in axisymmetric tension and compression do not provide the complete range of saturation conditions for other multi-axial remanent strain states.

By implementing the micromechanical model of Huber et al. (1999), Landis (2003) was able to map out the full range of remanent strain saturation states. Fig. 1 illustrates the remanent strain states that are possible in a ferroelastic polycrystal comprised of unpoled randomly oriented single crystal grains with tetragonal crystal structure. Remanent strain states that are below the curve are possible in the material, while those above the curve are unattainable. The following procedure has been proposed by Landis (2003) to determine when saturation is approached. First, since the remanent strain due to domain switching is volume conserving, the following two remanent strain invariants can be used to describe any multi-axial remanent strain state.

$$J_2^e = \left(\frac{2}{3} e_{ij}^r e_{ij}^r\right)^{1/2} \quad \text{and} \quad J_3^e = \left(\frac{4}{3} e_{ij}^r e_{jk}^r e_{ki}^r\right)^{1/3}. \quad (2.5)$$

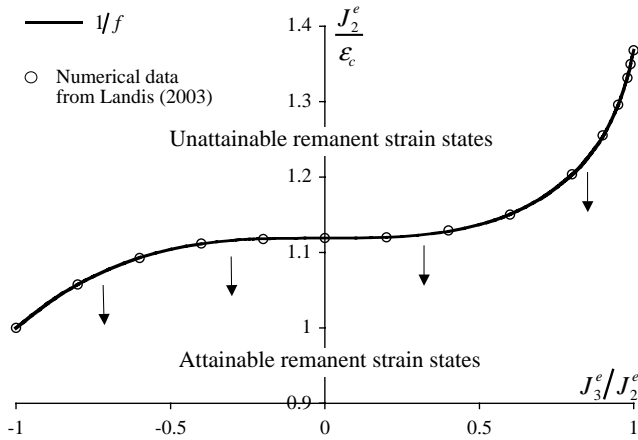


Fig. 1. The remanent strain saturation curve dividing remanent strain space into regions that are attainable and unattainable by a polycrystal assembled from randomly oriented tetragonal single crystals. Only remanent strain states below the curve are attainable by such a material. The dots are numerical results from Landis (2003) obtained using a micromechanical self-consistent model, and the line is one divided by the function f given in Eqs. (2.7) and (2.8). The remanent strain invariants J_2^e and J_3^e are defined in Eq. (2.5) and the results are normalized by the saturation strain in axisymmetric compression ϵ_c .

Here, e_{ij}^r is the remanent strain deviator, $e_{ij}^r = e_{ij}^r - \delta_{ij} e_{kk}^r / 3$. Due to volume conservation, the introduction of the remanent strain deviator appears to be unnecessary. However, the potential Ψ^r will be described with these two invariants, and the derivatives of Ψ^r with respect to e_{ij}^r will be affected by the distinction between the remanent strain and its deviator. With the definition of these two invariants, a full range of remanent strain saturation states can be probed by allowing the ratio of J_3^e / J_2^e to vary from -1 (axisymmetric contraction) to 0 (pure shear) to 1 (axisymmetric extension).

Now, define a strain-like variable $\bar{\epsilon}$ as

$$\bar{\epsilon} = J_2^e f(J_3^e / J_2^e), \tag{2.6}$$

where

$$f\left(\frac{J_3^e}{J_2^e}\right) = -0.0965 \left(\frac{J_3^e}{J_2^e}\right)^3 + 0.01 \left(\frac{J_3^e}{J_2^e}\right)^6 + 0.8935 \quad \text{for} \quad \left(\frac{J_3^e}{J_2^e}\right) < 0 \tag{2.7}$$

and

$$f\left(\frac{J_3^e}{J_2^e}\right) = -0.1075 \left(\frac{J_3^e}{J_2^e}\right)^3 - 0.027 \left(\frac{J_3^e}{J_2^e}\right)^6 - 0.028 \left(\frac{J_3^e}{J_2^e}\right)^{21} + 0.8935 \quad \text{for} \quad \left(\frac{J_3^e}{J_2^e}\right) \geq 0. \tag{2.8}$$

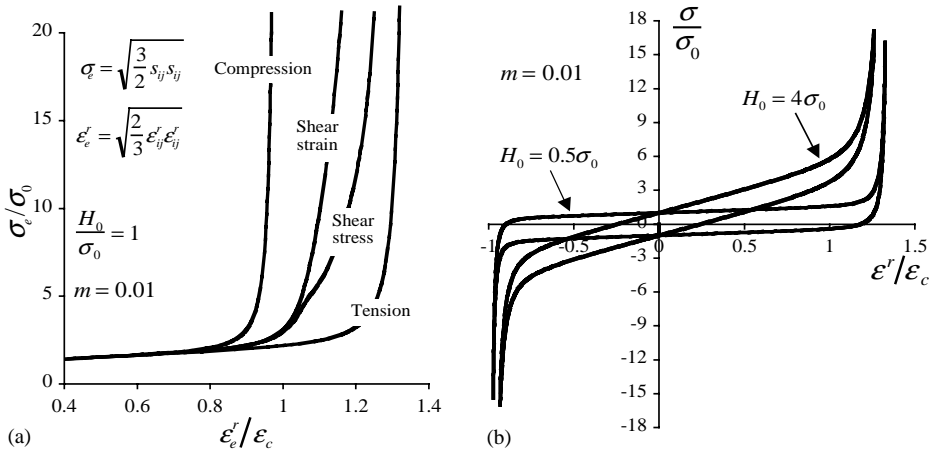


Fig. 2. (a) Effective stress versus effective remanent strain curves for the model material described in Section 2 in uniaxial compression, pure shear strain, pure shear stress and uniaxial tension tests. (b) Uniaxial stress versus remanent strain hysteresis loops for the model material illustrating the effect of the hardening parameter H_0 . In both cases notice the asymmetry in the remanent strains that can be achieved in tension versus compression.

Here, f is a functional fit to the numerical results obtained from the micromechanical computations described in Landis (2003). This fit is illustrated in Fig. 1. When the remanent strain level characterized by $\bar{\epsilon}$ reaches the compressive saturation level, ϵ_c , the remanent strain will be saturated. In other words, the only possible remanent strain states in the material are those that satisfy $\bar{\epsilon} \leq \epsilon_c$. Hence, in order to prohibit remanent strain states characterized by $\bar{\epsilon} > \epsilon_c$, the remanent potential Ψ^r must increase without bound as $\bar{\epsilon} \rightarrow \epsilon_c$.

Two final considerations were used to establish the functional form for Ψ^r . First, the potential should yield smooth stress versus strain behavior as the remanent strain goes through zero. Second, the functional form should be simple so that a parametric study can be readily performed within the fracture model. These criteria have been implemented to make the following choice for the remanent potential,

$$\Psi^r = \frac{1}{2} H_0 \epsilon_c \left[\frac{J_2^e}{\epsilon_c} \exp\left(\frac{m}{1 - \bar{\epsilon}/\epsilon_c}\right) \right]^2 \tag{2.9}$$

Here, H_0 is a characteristic level of back stress that primarily affects the initial slope of the uniaxial stress versus remanent strain curve, and m is another hardening parameter that controls how abruptly the strain saturation conditions are reached. Fig. 2a illustrates the predictions of the effective stress versus the effective remanent strain from the constitutive law for uniaxial compression, pure shear strain, pure shear stress and uniaxial tension. It is interesting to note that the shear strain and shear stress curves do not coincide. This feature is due to the fact that the material can strain more in tension than in compression, and has been confirmed in micromechanical simulations,

Landis (2003). Fig. 2b illustrates the uniaxial stress versus remanent strain hysteresis curves for two different sets of the material parameters H_0 and m .

With the remanent potential specified, it is possible to derive the back stresses and finally solve for the plastic multiplier yielding the incremental form of the constitutive law. For the implementation within the finite element model presented in the next section, a backward Euler integration scheme was developed such that the switching surface of Eq. (2.2) and the discretized version of the flow rule in Eq. (2.3) are satisfied at the end of the increment. Details of the backward Euler integration scheme are included in Appendix A.

3. The fracture model

Throughout this paper it is assumed that the applied loading is small enough such that the height of the switching zone around the crack is small compared to the length of the crack or any other specimen length dimension. Furthermore, only stress fields symmetric with respect to the crack plane will be analyzed, i.e. mode I loading. As discussed by Rice (1968), under these conditions a small-scale switching analysis can be performed on a semi-infinite crack with the remote applied stress field being that of the mode I asymptotic elastic K-field,

$$\begin{Bmatrix} \sigma_{11} \\ \sigma_{22} \\ \sigma_{12} \end{Bmatrix} \rightarrow \frac{K_I}{\sqrt{2\pi r}} \cos \frac{\theta}{2} \begin{Bmatrix} 1 - \sin \frac{\theta}{2} \sin \frac{3\theta}{2} \\ 1 + \sin \frac{\theta}{2} \sin \frac{3\theta}{2} \\ \sin \frac{\theta}{2} \cos \frac{3\theta}{2} \end{Bmatrix} \quad \text{as } r \rightarrow \infty. \tag{3.1}$$

Here K_I is the remote applied mode I stress intensity and r and θ are polar coordinates centered on the crack tip. Under plane strain conditions, K_I is related to the remote applied energy release rate G by

$$G = \frac{1 - \nu^2}{E} K_I^2. \tag{3.2}$$

Consider stable crack growth conditions such as a double cantilever beam specimen loaded by forcing a wedge along the crack growth direction. Initially the crack tip is stationary. As the loading is increased from zero, a localized zone of domain switching surrounds the crack tip. The characteristic half-height of the switching zone R_s under plane strain small-scale switching conditions (see Hutchinson, 1979, p. 14) is given as

$$R_s = \frac{1}{3\pi} \left(\frac{K_I}{\sigma_0} \right)^2 = \frac{1}{3\pi} \frac{GE}{(1 - \nu^2)\sigma_0^2}. \tag{3.3}$$

The crack tip will remain stationary and the switching zone size will continue to grow until some criterion for crack growth is met. In this paper, it is assumed that crack growth occurs when the crack tip energy release rate, G_{tip} , reaches a material specific critical level of G_0 . Such a “point” fracture criterion is an approximation to a more realistic extended fracture process zone. However, for crack growth initiation, the

critical crack tip energy release rate growth criterion is consistent with a crack plane cohesive force model as long as the cohesive zone size meets small-scale yielding conditions, Rice (1968). Furthermore, this consistency is also achieved under steady crack growth conditions if the extent of the cohesive process zone is small compared to the size of the region near the crack tip where strain saturation occurs. Applying an analogy to the mode III problem, the size of the saturation zone is approximately $R_{\text{sat}} \approx (\sigma_0/E\varepsilon_c)(GE/\sigma_0^2)$, Landis (2002b). Then, the size of the cohesive zone is $R_c \approx G_{\text{tip}}E/\sigma_c^2$ where σ_c is the peak cohesive strength. For properties characteristic of ferroelectrics, the results to be presented later suggest that $E\varepsilon_c/\sigma_0$ is of the same order of magnitude as G/G_{tip} during steady crack growth. Hence, the size of the cohesive zone will be much smaller than the size of the strain saturation zone if $\sigma_c^2 \gg \sigma_0^2$. For the fracture process of atomic decohesion, this condition is certainly satisfied.

Given this crack growth criterion and assuming that any non-proportional loading effects near a stationary crack in these materials can be neglected, the path-independence of the J -integral implies that $G_{\text{tip}} = G$ and crack growth will commence when $G = G_0$. This point corresponds to the crack growth initiation toughness on the R-curve for the material in consideration. Then, when the crack advances, material elements near the crack tip will unload or load in a non-proportional manner resulting in dissipated energy that must be supplied by the external loading in order to maintain crack growth. Hence, after initiation K_I and G must continue to increase until steady growth conditions are met. This behavior corresponds to the rising portion of the R-curve and occurs over a crack growth range of a few times the maximum switching zone height. After a considerable amount of crack growth, the switching zone and wake of switched material become well-developed and crack growth continues at a constant level of K_I or G . This corresponds to the plateau on the R-curve where steady-state crack growth occurs. The constant level of applied energy release rate during steady crack growth will be denoted as G_{ss} .

The analysis presented in this paper will focus only on the toughening due to domain switching during the steady crack growth conditions described above. Under steady growth conditions, all increments of field quantities can be related to derivatives with respect to the x_1 coordinate direction by

$$\dot{\phi} = -\dot{a} \frac{\partial \phi}{\partial x_1}. \quad (3.4)$$

Here, ϕ is any scalar field quantity such as a Cartesian component of stress or strain, and \dot{a} is the increment of crack advance in the x_1 direction. Finally, Hutchinson (1974) derived the following path-independent integral that can be used to determine the crack tip energy release rate G_{tip} during steady crack growth,

$$G_{\text{tip}} = I \equiv \int_{\Gamma} (Un_1 - \sigma_{ij}n_j u_{i,1}) d\Gamma, \quad (3.5)$$

where Γ is a counterclockwise directed contour encircling the crack tip, n_i are the components of the unit normal directed to the right along the contour, u_i are the components of the displacement vector, and U is the history dependent stress work

density at a material point defined by

$$U = \int_0^\epsilon \sigma_{ij} d\epsilon_{ij}. \tag{3.6}$$

In order to determine the amount of switch toughening that can occur in a given material, the stress and strain fields near a steadily growing crack must be computed. Due to the complex non-linear character of the ferroelastic constitutive law described in Section 2, these fields cannot be determined analytically and instead, they will be computed numerically with the finite element method. The numerical model to be used here was originally developed by *Dean and Hutchinson (1980)* and has been used by numerous authors to investigate steady crack growth in dissipative materials including conventional elastic–plastic, strain-gradient plastic, and visco-plastic materials among others. The basic idea of the formulation is that the finite element mesh is fixed to the crack tip and the material moves through the mesh from $x_1 = \infty$ to $-\infty$. The virtual work expression used to derive the finite element method is

$$\int_V \delta \epsilon_{ij} C_{ijkl} \epsilon_{kl} dV = \int_S \delta u_i T_i dS + \int_V \delta \epsilon_{ij} C_{ijkl} \epsilon_{kl}^r dV, \tag{3.7}$$

where S is the boundary of the volume V , C_{ijkl} are the Cartesian components of the isotropic elastic stiffness tensor that can be written in terms of E and ν , and the tractions acting on the boundary S are given as $T_i = \sigma_{ji} n_j$. These tractions are determined from the stress field of Eq. (3.1).

After insertion of the appropriate finite element interpolations, the left-hand side of this equation yields a standard linear elastic stiffness matrix dotted with the vector or unknown nodal displacements. The first term on the right is a vector of applied forces, and the last term is a residual body force vector that accounts for the remanent strain in the volume. An iterative procedure is applied to solve the non-linear steady crack growth problem. Initially it is assumed that the remanent strain at every point in the body is zero. Hence, the body force vector due to the remanent strains is zero and the linear elastic asymptotic crack tip field solution is recovered. With this solution, the constitutive law of Section 2 is integrated along streamlines of constant height above the crack plane from the right edge of the finite element mesh to the left. This integration yields a new approximation for the distribution of remanent strains. The residual body force vector is recomputed and a new nodal displacement solution is calculated. Again, the constitutive law is integrated along streamlines to obtain a new distribution of remanent strains and the procedure is repeated until the solution achieves a suitable level of convergence.

Within this model for fracture of ferroelastic materials, dimensional analysis and manipulation of the constitutive law dictate that the normalized stresses and strains will be of the forms

$$\frac{\sigma_{ij}}{\sigma_0} = \bar{\sigma}_{ij} \left(\frac{x_1}{R_s}, \frac{x_2}{R_s}, \frac{\epsilon_c E}{\sigma_0}, \frac{H_0}{\sigma_0}, m, \nu \right), \tag{3.8}$$

$$\frac{\epsilon_{ij}}{\epsilon_c} = \bar{\epsilon}_{ij} \left(\frac{x_1}{R_s}, \frac{x_2}{R_s}, \frac{\epsilon_c E}{\sigma_0}, \frac{H_0}{\sigma_0}, m, \nu \right), \tag{3.9}$$

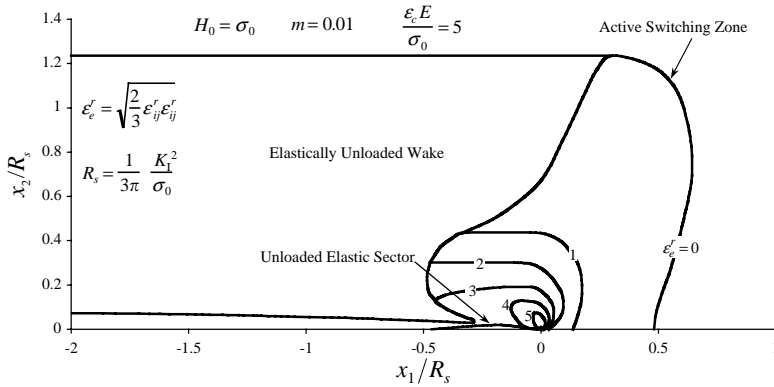


Fig. 3. The distribution of effective remanent strain near a growing crack in a ferroelastic material. The active switching zone, elastically unloaded wake, and unloaded elastic sector behind the crack tip are each denoted on the illustration. The material law is given in Section 2, and the material parameters for this computation are $\epsilon_c E/\sigma_0 = 5$, $H_0 = \sigma_0$, $m = 0.01$ and $\nu = 0.25$.

where $\bar{\sigma}_{ij}$ and $\bar{\epsilon}_{ij}$ are dimensionless functions of the normalized spatial coordinates parameterized by the normalized material quantities. Here R_s is the characteristic size of the steady-state switching zone given by Eq. (3.3) when $G = G_{ss}$. Also note that R_s is the only characteristic length appearing in the model that can be used to normalize the spatial dimensions. Finally, the relative toughening ratio will only depend on the dimensionless material parameters, i.e.

$$\frac{G}{G_{tip}} = \frac{G_{ss}}{G_0} = \bar{G} \left(\frac{\epsilon_c E}{\sigma_0}, \frac{H_0}{\sigma_0}, m, \nu \right). \tag{3.10}$$

Eq. (3.10) reinforces that in this model, crack growth occurs when the crack tip energy release rate, G_{tip} , reaches some material specific critical level G_0 .

3.1. Results

Prior to presenting results for the toughening ratio, some features of the distributions of stress and remanent strain fields will be given. Due to the mode I symmetry of the problem only the upper half plane needs to be analyzed. Fig. 3 is a contour plot of the effective strain distribution near a steadily growing crack in a ferroelastic material. As a material point approaches the crack tip from the right, switching commences as it enters the active switching zone. Very close to the crack tip the remanent strain of such a material point will accumulate, reorient as the crack tip passes, and eventually the material point will unload elastically. The active switching zone is the region where remanent strain is accumulating or reorienting, while in the unloaded wake the remanent strain distributions are uniform in the x_1 -direction. The shape of the active switching zone is very similar to the shape of the active plastic zone near a steadily growing crack in an elastic-perfectly plastic material, [Dean and Hutchinson](#)

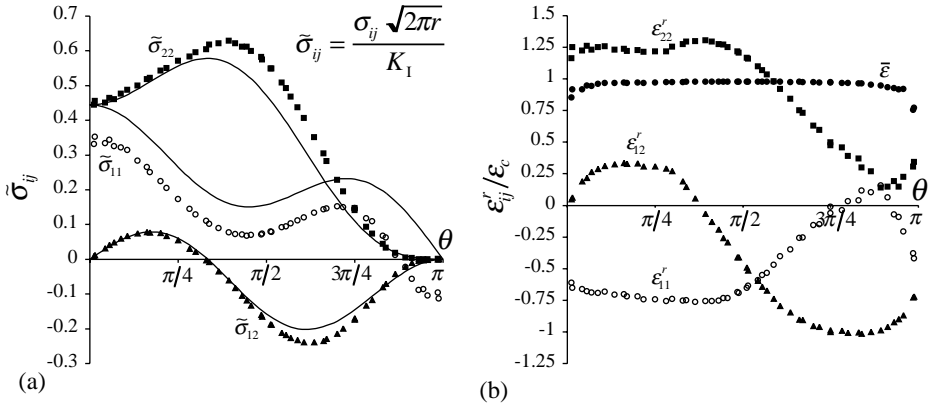


Fig. 4. (a) The angular distribution of the stresses very close to the crack tip. The dots are numerical results for a material with $\epsilon_c E / \sigma_0 = 3$, $H_0 = 0.1 \sigma_0$, $m = 0.01$ and $\nu = 0.25$, and the solid lines are the result for an isotropic elastic solid. Note that the $1/\sqrt{r}$ radial dependence has been accounted for within the normalization. (b) The angular distribution of remanent strains very close to the crack tip from the same computation. The numerical results plotted in both figures are for all integration stations within the radial range $8 \times 10^{-3} R_s < r < 1.3 \times 10^{-2} R_s$.

(1980), Landis et al. (2000). One significant difference between the active zones in these two types of materials is that in the ferroelastic material the unloaded elastic sector behind the crack tip actually lies along the crack faces, while the same feature in the perfectly plastic material is tilted away from the crack faces. Another significant difference between the ferroelastic and perfectly plastic material is that remanent strains in the ferroelastic material are bounded, while plastic strains in the perfectly plastic material are unbounded near the crack tip.

Due to the strain saturation effect, the stresses near the crack tip in the ferroelastic material increase severely. In fact, the numerical results suggest that very close to the crack tip the stresses have a $1/\sqrt{r}$ radial dependence. Hence the crack tip stress intensity factor $K_{I \text{ tip}}$ can be defined such that on the plane ahead of the crack tip $\sigma_{yy} \rightarrow K_{I \text{ tip}} / \sqrt{2\pi r}$ as $r \rightarrow 0$. However, the results also suggest that angular dependence of the stress field asymptotically close to the crack tip is *not* equivalent to the asymptotic field for an isotropic elastic solid. The discrepancy between the ferroelastic asymptotic field and the isotropic elastic asymptotic field is most pronounced for low values of H_0 / σ_0 and large values of $\epsilon_c E / \sigma_0$. Fig. 4a plots the angular dependence of the stresses near a growing crack tip in a ferroelastic material with properties $\epsilon_c E / \sigma_0 = 3$, $H_0 = 0.1 \sigma_0$, $m = 0.01$ and $\nu = 0.25$. Notice that the $1/\sqrt{r}$ radial dependence of the stresses has been accounted for in the normalization. Furthermore, since the stresses do not follow the isotropic asymptotic field, the relationship between G_{tip} and $K_{I \text{ tip}}$ is *not* given by Eq. (3.2). This then implies that $G / G_{\text{tip}} \neq (K_I / K_{I \text{ tip}})^2$ within these simulations. Specifically, for the material parameters used in Fig. 4, $G / G_{\text{tip}} = 3.02$ whereas $K_I / K_{I \text{ tip}} = 2.25$. For comparison, if the hardening parameter is changed to $H_0 = 10 \sigma_0$, then the stress field is very close to the isotropic asymptotic field (the σ_{11} component falls noticeably but

just slightly below the isotropic curve) and $G/G_{\text{tip}} = 1.29$ with $K_I/K_{I\text{tip}} = 1.20$. A similar approach of the asymptotic ferroelastic stresses to the isotropic elastic asymptotic fields occurs as $\varepsilon_c E/\sigma_0 \rightarrow 0$, which is to be expected.

Fig. 4b plots the angular dependence of the remanent strains near the growing crack tip in the same material described above. Note in Fig. 4b that the saturation strain variable $\bar{\varepsilon}$ is very close to ε_c over the entire angular range, denoting that the material is in fact near saturation close to the crack tip. However, the remanent strain components are not uniform, indicating that remanent strain reorientation does occur around a growing crack. A more accurate determination of the near tip ferroelastic asymptotic fields and a verification of the numerical results presented here could be carried out via a detailed asymptotic analysis along the lines of Ponte Castañeda (1987). However, such an analysis will not be presented here.

The primary goal of this fracture model is to determine how the steady-state toughness enhancement in ferroelastic materials, G_{ss}/G_0 , depends on the material properties. Eq. (3.9) identifies the material properties in question and also ranks them in order of significance. Poisson's ratio ν will be shown to have a very weak influence over the toughness enhancement. The two hardening parameters, H_0/σ_0 and m , have a much stronger influence on G_{ss}/G_0 , and it will be shown that as the hardness of the material increases then the toughness enhancement decreases. Finally, the most fundamental material parameter that has been identified in all transformation toughening models is $\varepsilon_c E/\sigma_0$. Explicitly, this is the ratio of the irreversible strain to the characteristic elastic strain in the material. However, if this ratio is rearranged as $(\sigma_0 \varepsilon_c)/(\sigma_0^2/E)$, then it can also be interpreted as the ratio of the characteristic level of dissipated to stored energy in the material. Results for the dependence of G_{ss}/G_0 with respect to $\varepsilon_c E/\sigma_0$ will be given presently.

Fig. 5 plots G_{ss}/G_0 versus $\varepsilon_c E/\sigma_0$ for a range of initial hardening values H_0/σ_0 with $m = 0.01$ and $\nu = 0.25$. The first observation to make about this plot is that the toughness enhancement increases monotonically as the saturation level of irreversible remanent strain increases. Larger relative saturation strains imply that the material can dissipate more energy, which in turn implies higher steady-state fracture toughness. A second feature illustrated on this plot is the dependence on the hardening parameter H_0/σ_0 . As shown in Fig. 2b, increasing levels of H_0/σ_0 induce higher stresses in the material which are required to reach given levels of remanent strain. This in turn impedes switching near the crack tip and reduces the level of switch toughening. Fig. 5 illustrates that there is a relatively strong dependence of the toughness enhancement on the initial hardness ratio H_0/σ_0 . Hence, the actual shape of the stress strain curve in these materials is important when making a quantitative determination of the fracture toughness. Finally, it is worth noting that these toughness curves are relatively straight at low levels of $\varepsilon_c E/\sigma_0$. Therefore, the initial slope of these curves when $\varepsilon_c E/\sigma_0 = 0$ provides a useful measure of the toughness enhancement. Specifically, the toughening parameter α is defined as

$$\alpha \equiv \frac{\sigma_0}{G_0 E} \left. \frac{\partial G_{\text{ss}}}{\partial \varepsilon_c} \right|_{\varepsilon_c=0}. \quad (3.11)$$

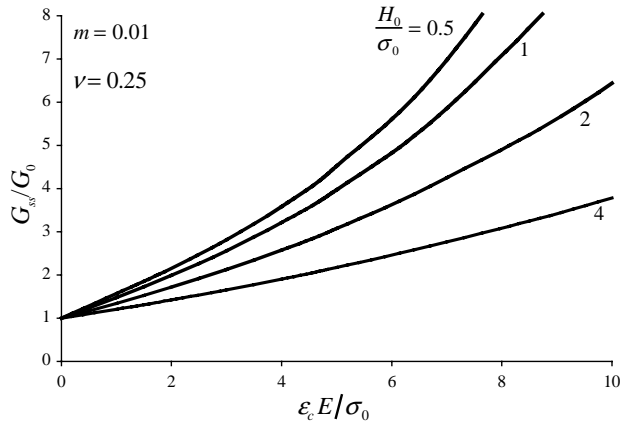


Fig. 5. The toughness enhancement, G_{ss}/G_0 , during steady crack growth in a ferroelastic material as a function of the saturation strain level, $\epsilon_c E/\sigma_0$, for a range of initial hardening values, H_0/σ_0 .

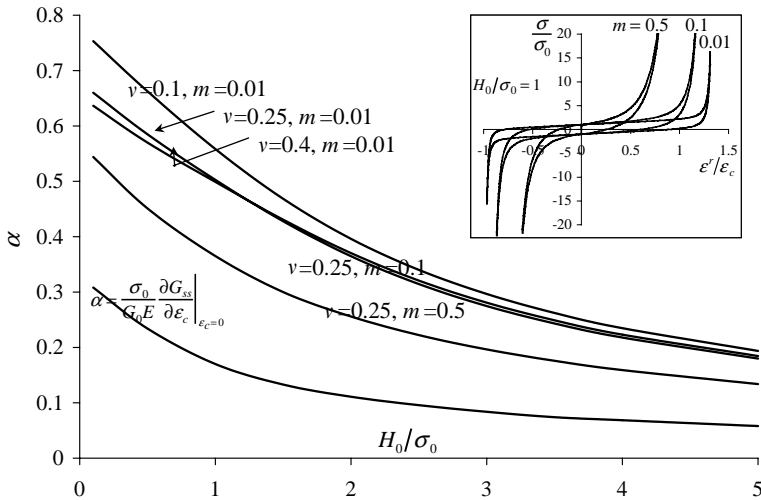


Fig. 6. The initial slope of the toughness ratio versus the relative saturation strain, α , as a function of the initial hardening H_0/σ_0 , for a range of Poisson's ratio and m . The insert plots hysteresis loops in order to illustrate the dependence of the stress–strain behavior on m .

Fig. 6 plots the toughening parameter α as a function of H_0/σ_0 for ranges of Poisson's ratio and the second hardening parameter m . The insert plots hysteresis loops for a few values of m and a single value of $H_0/\sigma_0=1$. First notice that α is only weakly dependent on Poisson's ratio, and this dependence is very weak for the range of $0.25 < \nu < 0.4$. The toughness enhancement has a stronger dependence on the hardening parameter m .

However, note from the inset in Fig. 6 that increasing m drastically increases the stress levels near strain saturation. Effectively, large m values reduce the saturation strain of the material. It is likely that most materials are characterized within the range of $0 < m < 0.1$.

In summary, results from numerical computations of the stress and strain fields and the toughness enhancement during steady crack growth in ferroelastic materials have been presented. The computations illustrate a few interesting features and confirm some intuitive hypotheses about the solutions. First, the near tip stresses appear to recover a $1/\sqrt{r}$ singular form, however the angular dependencies of these stresses is not identical to those for an isotropic elastic material. It was also shown that the distributions of remanent strain are not trivial, and do reorient as the crack tip passes. Lastly, as would be expected, the steady-state toughness of the material increases as the relative saturation strain increases, and decreases as the initial hardening slope of the material increases.

4. Approximate models

4.1. Semi-analytical models

Two types of approximate models for the toughness enhancement in ferroelastic materials will be presented in this section. The first, which has been used by Freund and Hutchinson (1985) to investigate high strain-rate crack growth, applies the I -integral of Eq. (3.4) to analyze G_{tip} . Applying the path-independence of I , Hutchinson (1974) showed that

$$G_{\text{tip}} = G - \int_{-h}^h U^* dx_2, \quad (4.1)$$

where

$$U^*(x_2) = \lim_{x_1 \rightarrow -\infty} U(x_1, x_2) \quad (4.2)$$

and h is the half-height of the switching zone. The integral in Eq. (4.1) accounts for all of the energy dissipated by the material in the switching zone, along with any energy stored by residual stresses in the wake.

If the distributions of stress and strain in the material are known a priori, then Eq. (4.1) can be analyzed to determine the relationship between G and G_{tip} . However, in general the field distributions are not known, and this is the reason why the problem must be solved numerically as in Section 3. Although, when the saturation strains are small, the approximation can be made that the stress fields given by Eq. (3.1) are valid everywhere. Given these stress fields, the constitutive law of Section 2 is integrated along streamlines of constant height above the crack plane to determine the strains, and then Eq. (4.1) can be evaluated numerically. This form of the model will be termed the *assumed stress semi-analytical model* (S-A Stress in Fig. 8).

Instead of making assumptions about the stresses, it is equally valid to assume that the elastic strain fields derived from the stresses in Eq. (3.1) remain unchanged. In this case the constitutive law is integrated to determine the corresponding stresses, and once again Eq. (4.1) can be evaluated. This form of the model will be referred to as the *assumed strain semi-analytical model* (S-A Strain in Fig. 8). Due to the complexity of the constitutive law of Section 2, all of the integrations described above must be carried out numerically. This is unfortunate, but it will be shown that the results of these models have the same initial slope on the toughness ratio versus relative saturation strain curves as the accurate finite element results presented in Section 3. Hence, these two models yield accurate quantitative results for the toughening parameter α without the need to solve the full non-linear boundary value problem.

4.2. Analytical models

Due to the need for numerics, the models described above are referred to as semi-analytical. The second type of approximate models to be presented here will be referred to as analytical, since closed form expressions for the toughness enhancement due to switching can be determined from them. These models are akin to the transformation toughening analysis performed by [McMeeking and Evans \(1982\)](#). The model can be stated as follows. First it is assumed that the stress fields of Eq. (3.1) are valid. Hence, these models are most applicable when the transformation strains are small. As the crack tip approaches a material point, transformation occurs at a critical level of stress. When this stress is achieved, the material point accumulates a finite pre-determined level of transformation strain (the orientation of the transformation strain can be determined by the stress state). As the crack continues to grow, the material point maintains its original transformation strain as it traverses to $x_1 \rightarrow -\infty$. Hence, the entire distribution of transformation strain is determined by the stress state at the frontal boundary of the transformation zone. This semi-infinite strip of transformed material places closure stresses on the crack tip and reduces the crack tip stress intensity factor by ΔK_I .

Conceptually, the effects of the transformation zone on the crack tip stress intensity factor can be treated as follows. First, allow every point in the transformation zone to freely expand or contract by the appropriate transformation strain. Note that this transformation strain can vary with position in the x_2 direction. Next, apply appropriate body forces and surface tractions to transformation zone such that the total strains everywhere are returned to zero. Finally, place this constrained transformation zone back into the surrounding material and remove the applied body forces and surface tractions. Then, weight function methods can be applied to determine the decrease in crack tip stress intensity ΔK_I , [Rice \(1972\)](#). Specifically,

$$\Delta K_I = \int_{\Gamma} t_i h_i d\Gamma + \int_A b_i h_i dA, \quad (4.3)$$

where A is the region where transformation has occurred and Γ is its boundary. The body force components b_i and surface traction components t_i are the *opposite* of those

required to negate the transformation strains. In plane strain the weight functions are

$$h_1 = \frac{1}{4(1-\nu)\sqrt{2\pi r}} \left[-2(1-2\nu) \cos \frac{\theta}{2} + \sin \theta \sin \frac{3\theta}{2} \right], \quad (4.4)$$

$$h_2 = \frac{1}{4(1-\nu)\sqrt{2\pi r}} \left[4(1-\nu) \sin \frac{\theta}{2} - \sin \theta \cos \frac{3\theta}{2} \right]. \quad (4.5)$$

Then, for a deviatoric transformation strain, the traction and body force are given as

$$t_i = \frac{E}{1+\nu} \varepsilon_{ij}^T n_j, \quad (4.6)$$

$$b_i = -\frac{E}{1+\nu} \varepsilon_{ij,j}^T. \quad (4.7)$$

Finally, Eqs. (4.6) and (4.7) can be applied in Eq. (4.3) along with the divergence theorem to yield

$$\Delta K_I = \frac{E}{1+\nu} \int_A \varepsilon_{ij}^T h_{i,j} dA. \quad (4.8)$$

Note that the crack tip stress intensity factor is then just the sum of the applied stress intensity factor and ΔK_I , i.e.

$$K_{I \text{ tip}} = K_I + \Delta K_I. \quad (4.9)$$

To analyze Eq. (4.8) a transformation criterion and “flow rule” are required to determine A and ε_{ij}^T . The choice of these parameters that is most consistent with the constitutive model of Section 2 is that transformation occurs when the effective stress reaches the switching strength and the transformation strain is in the direction of the stress deviator, i.e.

$$\varepsilon_{ij}^T = \frac{3}{2} \frac{\varepsilon_0}{\sigma_0} s_{ij} \quad \text{when} \quad \sigma_e \equiv \sqrt{\frac{3}{2} s_{ij} s_{ij}} = \sigma_0. \quad (4.10)$$

Here, the magnitude of the transformation strain ε_0 should be taken to be between ε_c and $1.37\varepsilon_c$. This model was solved for the full range of Poisson’s ratios, however it can only be solved analytically when $\nu = 0.5$. It is noted that there is a weak but non-monotonic dependence of ΔK_I on ν in the range of $0 \leq \nu \leq 0.5$. This model will be referred to as A1 (first analytical model) in Fig. 8. The analytic solution for $\nu = 0.5$ is outlined below.

Within these types of analytical toughening models, it is assumed that switching itself does not perturb the size or shape of the switching zone. Hence, the frontal boundary of the switching zone is found by determining where the stress fields given by Eqs. (3.1) just meet the switching criterion. As noted above, switching occurs when $\sigma_e = \sigma_0$ for this first analytical model. For $\nu = 0.5$ the frontal boundary of the switching zone is given as

$$R(\theta) = \frac{3}{8\pi} \left(\frac{K_I}{\sigma_0} \right)^2 \sin^2 \theta \quad \text{for} \quad -\frac{\pi}{2} \leq \theta \leq \frac{\pi}{2}. \quad (4.11)$$

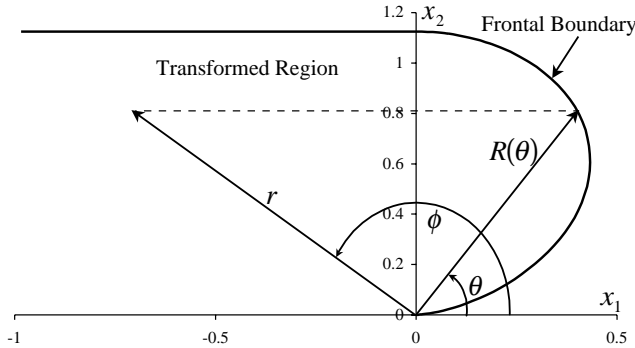


Fig. 7. An illustration of the variables used to evaluate the integrals arising in the analysis of the analytical models. The frontal boundary illustrated is that for transformation occurring at a critical level of effective stress with Poisson’s ratio equal to one half. Note that during the evaluations of the integrals, the integration over the x -coordinate is carried out first.

Then, the area integral of Eq. (4.8) can be shown to be equal to

$$\begin{aligned} \Delta K_I &= \frac{\sqrt{3}}{2\sqrt{2\pi}} E \varepsilon_0 \int_A \frac{1}{r^{3/2}} \cos \frac{3\theta - 5\phi}{2} \sin \phi \, dA \\ &= K_I \frac{E \varepsilon_0}{\sigma_0} \frac{9}{4\pi} \int_0^{\pi/2} \cos \theta \sqrt{\sin \theta} \left(\int_\theta^\pi \sqrt{\sin \phi} \cos \frac{3\theta - 5\phi}{2} \, d\phi \right) d\theta \\ &= - \underbrace{\frac{1}{2\pi} \frac{\varepsilon_0}{\varepsilon_c}}_{\alpha/2} \frac{E \varepsilon_c}{\sigma_0} K_I \quad \text{for } \nu = 0.5. \end{aligned} \tag{4.12}$$

Fig. 7 illustrates the variables, r , θ , and ϕ that were used to carry out the integration over the area of the transformed region. The frontal boundary illustrated in Fig. 7 is the actual boundary shape for $\nu = 0.5$. As mentioned previously, due to the assumption that the transformation itself does not perturb the location of the transformation boundary, this type of model is most valid for small transformation strains. Within the small transformation strain range, the toughening ratio can be expanded into a Taylor series with respect to $\varepsilon_0 E / \sigma_0$ as

$$\frac{G}{G_{\text{tip}}} = \left(\frac{K_I}{K_{I\text{tip}}} \right)^2 \approx 1 + \frac{1}{\pi} \frac{E \varepsilon_0}{\sigma_0} \quad \text{or} \quad \alpha = \frac{1}{\pi} \frac{\varepsilon_0}{\varepsilon_c} \approx 0.32 - 0.44. \tag{4.13}$$

Here the range on the toughening parameter α corresponds to taking $\varepsilon_0 = \varepsilon_c$ or $\varepsilon_0 = 1.37 \varepsilon_c$.

A model similar to this one has been presented previously by [Reece and Guiu \(2002\)](#), however a different switching criterion is used in that work. This model (A2 in Fig. 8) and its proper solution are presented here. [Reece and Guiu \(2002\)](#) assume that transformation occurs when the shear component of the crack tip stress field resolved at 45° to the crack plane reaches a critical value of τ_0 . To maintain continuity with the previous models, this critical level of shear stress will be taken to be $\tau_0 = \sigma_0 / \sqrt{3}$. Once this switching criterion is reached, a shear transformation strain occurs with magnitude

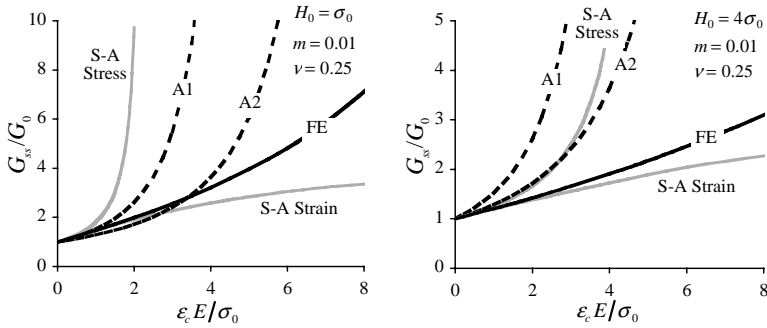


Fig. 8. A comparison of the semi-analytical (S-A stress and S-A strain) and analytical (A1 and A2) of Section 4 to the numerical finite element results (FE) of Section 3. S-A Stress and S-A Strain denote the semi-analytical model with either the assumed stress or strain field, respectively. A1 denotes the analytical model with the effective stress transformation criteria and flow rule of Eq. (4.10), and A2 denotes the analytical model of Reece and Guin (2002). (a) Plots the comparisons for $H_0/\sigma_0 = 1$. (b) Plots the comparisons for $H_0/\sigma_0 = 4$. Note that the semi-analytical models always have the same initial tangent as the finite element results, while the analytical models cannot account for dependencies on the material hardness.

γ_0 along the 45° planes. Again, to maintain continuity with the previous model, the transformation shear strain will be taken as $\gamma_0 = \sqrt{3}\epsilon_0$. Then, the frontal boundary of the transformation zone and the transformation strain field are

$$R(\theta) = \frac{3}{8\pi} \left(\frac{K_I}{\sigma_0} \right)^2 \sin^2 \theta \sin^2 \left(\frac{3\theta}{2} \right) \quad \text{for } -\frac{2\pi}{5} \leq \theta \leq \frac{2\pi}{5} \tag{4.14}$$

and

$$\epsilon_{11}^T = -\frac{\sqrt{3}\epsilon_0}{2}, \quad \epsilon_{22}^T = \frac{\sqrt{3}\epsilon_0}{2} \quad \text{and} \quad \epsilon_{12}^T = 0. \tag{4.15}$$

Note that the transformation strain field does not depend on the position along the frontal boundary. This feature differs from the previous analytical model. Now, ΔK_I can be computed as

$$\begin{aligned} \Delta K_I &= \frac{3\sqrt{3}}{16\sqrt{2\pi}} \frac{E\epsilon_0}{1-\nu^2} \int_A \frac{\cos 3\phi/2 - \cos 7\phi/2}{r^{3/2}} dA \\ &= \frac{K_I}{1-\nu^2} \frac{E\epsilon_0}{\sigma_0} \frac{27}{32\pi} \int_0^{2\pi/5} \sin \frac{5\theta}{2} \sqrt{\sin \theta} \left(\int_\theta^\pi \frac{\cos 3\phi/2 - \cos 7\phi/2}{\sqrt{\sin \phi}} d\phi \right) d\theta \\ &= - \underbrace{\frac{3 \sin^5(2\pi/5)}{8\pi}}_{\alpha/2} \frac{1}{1-\nu^2} \frac{\epsilon_0}{\epsilon_c} \frac{E\epsilon_c}{\sigma_0} K_I. \end{aligned} \tag{4.16}$$

This result applies for all values of Poisson's ratio, and yields values for α in the range of $\alpha = 0.25\text{--}0.34$ for $\nu = 0.5$ and $\alpha = 0.20\text{--}0.27$ for $\nu = 0.25$. Again, the ranges on α correspond to taking $\varepsilon_0 = \varepsilon_c$ or $\varepsilon_0 = 1.37\varepsilon_c$. It is noted that this result differs from that obtained by [Reece and Guiu \(2002\)](#) due to an erroneous analogy to the volumetric transformation strain problem used in that work.

Lastly, the relative toughness enhancements predicted by these two analytical models are in line with another rough estimate based on Eq. (4.1). If we make the approximation that U^* is the dissipated energy $\sigma_0\varepsilon_0$, then Eq. (4.1) yields an approximation for the crack tip energy release rate of $G_{\text{tip}} \approx G - 2\sigma_0\varepsilon_0h = G - 2\sigma_0\varepsilon_0R(\theta_{\text{max}}) \sin \theta_{\text{max}}$. For the critical effective stress (A1) model $\theta_{\text{max}} = \pi/2$ when $\nu = 0.5$, and for the Reece and Guiu model (A2) $\theta_{\text{max}} = 2\pi/5$ for all ν . Therefore, the approximation for the toughening parameter is then, $\alpha \approx \varepsilon_0/\pi\varepsilon_c$ when $\nu = 0.5$ for the A1 model and $\alpha \approx 3 \sin^5(2\pi/5)\varepsilon_0/4\pi(1 - \nu^2)\varepsilon_c$ for the A2 model. Interestingly, these two approximations are identical to the results reported in Eqs. (4.13) and (4.16). However, this agreement appears to be fortuitous, since no rigor was used to establish U^* within this last approximation. In fact, for the first model, exact agreement is not obtained for Poisson's ratios other than one half. However, ultimately the relative toughness enhancements predicted by these two analytical models can be related to the ratios of the predicted switching zone heights. Specifically, the toughness enhancement predicted by the analytical model of [Reece and Guiu \(2002\)](#) is approximately 20% smaller than that for the critical effective stress model. Furthermore, this difference in toughness enhancement is correlated with the predicted heights of the switching zones for each model, which also differs by approximately 20%.

4.3. Comparison of results

The results of the semi-analytical and analytical models presented in this section will now be compared to the finite element results of Section 3. Fig. 8 plots the comparisons of the approximate models of Section 4 with the accurate numerical computations of Section 3. S-A Stress and S-A Strain denote the semi-analytical assumed stress field and assumed strain field models described in Section 4.1. A1 denotes the analytical model with the effective stress transformation criterion and flow rule of Eq. (4.10), and A2 denotes the analytical model of [Reece and Guiu \(2002\)](#). Lastly, FE denotes the numerical finite element results. Recall that the semi-analytical models only make approximations about the stress or strain fields, but the constitutive response of the material is integrated accurately. In contrast, the analytical models make simplifying assumptions about both the stress fields near the crack tip and the constitutive response of the material. Hence, the analytical models cannot account for the shape of the stress strain curve while the semi-analytical models can. These features of the two types of approximate models are made clear by comparing Fig. 8a where $H_0/\sigma_0 = 1$ to Fig. 8b where $H_0/\sigma_0 = 4$. Note that in both figures the semi-analytical models have the same initial slope as the finite element results. However, the analytical models cannot incorporate any dependence on H_0/σ_0 and hence cannot predict the relationship between the toughening ratio and the material hardening slope.

The plots in Fig. 8 confirm that these approximate models are most accurate for small transformation strain ratios. In fact, the numerical results suggest that the *semi-analytical* models yield the correct values of the toughening parameter α , i.e. the initial slope of the G_{ss}/G_0 versus $\varepsilon_c E/\sigma_0$ curves. In this sense, the semi-analytical models are first order accurate, in that they predict the correct toughening enhancement to first order in $\varepsilon_c E/\sigma_0$, while the analytical models can only be considered zeroth order accurate. Furthermore, the calculations also suggest that the approximate models that apply an assumed stress field grossly overestimate the toughness enhancement for large $\varepsilon_c E/\sigma_0$, while the one model that implements the assumed strain field underestimates the steady-state toughness. For each of the models, the extrapolation

$$\frac{G_{ss}}{G_0} \approx 1 + \alpha_{\text{model}} \frac{\varepsilon_c E}{\sigma_0} \quad (4.17)$$

to large values of $\varepsilon_c E/\sigma_0$ always gives a superior estimate of the toughness enhancement than the explicit solution of the model itself. Finally, the following point is worth emphasis, the semi-analytical models that exercise the detailed constitutive law yield highly accurate (if not exact) values for the toughening parameter α for all shapes of the stress–strain behavior.

5. Discussion

The steady-state fracture toughness enhancement in ferroelastic ceramics has been computed accurately by implementing a micromechanically verified phenomenological constitutive law to describe the continuum material response. The constitutive law is able to account for most of the features of ferroelastic deformation, including the asymmetry in tensile versus compressive remanent strains and the Bauschinger effect. This constitutive law was implemented within the finite element method to determine the fields near a steadily growing crack. Crack growth was assumed to occur at a critical level of the crack tip energy release rate. The most significant material features that control the level of toughening in these materials have been identified as the relative saturation strain level and the shape of the uniaxial stress–strain curve.

Two types of approximate models were also presented in this work. Instead of solving a complete non-linear boundary value problem, as was done in the finite element computations, the approximate models assume that either the stress or the strain field from the asymptotic mode I isotropic elastic solution remains valid everywhere. It was found that the approximate models that apply the assumed stress field generally overestimate the toughness enhancement and the models using the assumed strain field underestimate G_{ss}/G_0 . For all of the approximate models, extrapolation of the initial slope of the toughness versus saturation strain curves to larger values of the saturation strain offered better toughness predictions than the accurate solution of the model itself. Finally, the semi-analytical models that implement Hutchinson's I -integral to compute the toughness enhancement are able to accurately predict the initial slope of the toughening curves for the full range of stress–strain curve shapes without the need to solve the full boundary value problem.

Due to the inherent brittleness of ferroelastic ceramics, there is a dearth of detailed experimental measurements on the full range of uniaxial stress–strain behavior. In tension, the material fractures before strain saturation can be achieved. Hence, most experiments in the literature are carried out in compression. This is unfortunate since even a partial hysteresis loop would be very useful for the determination of the switching strength. Specifically, the width of the hysteresis loop is approximately $2\sigma_0$. In order to obtain information from the uniaxial compressive stress–strain curve, the following observations are made. The elastic modulus should be taken as the initial slope of the *unloading* portion of the stress–strain curve. The compressive saturation strain is then at least as large as the strain extrapolated back to zero stress using this initial unloading slope. If the stress–strain behavior is measured on an electrically *poled* sample, then the non-linear strain range is approximately $2.37\varepsilon_c$. Finally, the slope of the switching portion of the stress–strain curve is approximately equal to H_0/ε_c . Applying these considerations to the data available in the literature, it was found that PZT materials have properties in the range $\varepsilon_c E/\sigma_0 \approx 3\text{--}7$ and $H_0/\sigma_0 \approx 1$, Schäufele and Härdtl (1996), and PLZT has properties near $\varepsilon_c E/\sigma_0 \approx 5$ and $H_0/\sigma_0 \approx 1$, Lynch (1996). Applying these material properties to the model computations of Section 3 the predicted steady-state toughness enhancement for these materials is in the range of $G_{ss}/G_0 \approx 2.5\text{--}5.8$ or $\Delta K_{Ic} \approx 60\text{--}140\%$. As mentioned in the Introduction, experimental investigations on unpoled ferroelectric ceramics by Meschke et al. (2000) for barium titanate and Lucato et al. (2000) and Oates et al. (2003) for PZT, have found toughness enhancements in the range of $\Delta K_{Ic} = 40\text{--}100\%$ of the initiation toughness. Hence, the model yields prediction in the appropriate range. A more critical experimental comparison can only be made if both fracture data and detailed stress–strain measurements are obtained for the same material.

Acknowledgements

The author would like to acknowledge support from the Army Research Office contract DAAD19-02-1-0241.

Appendix A

In order to perform the finite element computations of Section 3, a stable integration method for the constitutive law described in Section 2 must be available. To this end, use of a fourth order Runge–Kutta routine was attempted initially. However, this method failed since in many cases the routine would attempt to access derivative information from unattainable remanent strain states. The derivatives returned would either be infinities or physically meaningless. To solve this problem the following backward Euler integration routine was implemented.

We wish to satisfy the switching criterion and flow rule, Eqs. (2.2) and (2.3), at the end of the specified strain increment from the finite element solution. Hence, we have

$$\Delta \varepsilon_{ij}^r = \lambda (s_{ij} - s_{ij}^B). \quad (\text{A.1})$$

The plastic multiplier λ can be found by using the switching criterion of Eq. (2.2),

$$\begin{aligned} \Delta \varepsilon^r &= \sqrt{\frac{2}{3} \varepsilon_{ij}^r \varepsilon_{ij}^r} = \lambda \sqrt{\frac{2}{3} (s_{ij} - s_{ij}^B)(s_{ij} - s_{ij}^B)} = \frac{2}{3} \sigma_0 \lambda \\ \rightarrow \lambda &= \frac{3}{2} \frac{\Delta \varepsilon^r}{\sigma_0}. \end{aligned} \quad (\text{A.2})$$

Then, applying the elasticity law with μ as the isotropic shear modulus, we obtain nine (five independent) non-linear equations in terms of the remanent strain increments $\Delta \varepsilon_{ij}^r$.

$$f_{ij} = \frac{\sigma_0 \Delta \varepsilon_{ij}^r}{\Delta \varepsilon^r} - \frac{3}{2} [2\mu(e_{ij} - \varepsilon_{ij}^r|_t - \Delta \varepsilon_{ij}^r) - s_{ij}^B] = 0. \quad (\text{A.3})$$

The total strain deviator e_{ij} is known from the finite element solution, $\varepsilon_{ij}^r|_t$ is the remanent strain known from the previous step in the integration, and $\Delta \varepsilon_{ij}^r$ is the remanent strain increment deviator. Finally, note that s_{ij}^B are the components of the back stress deviator that depend on the remanent strain components at the end of the increment, i.e. $s_{ij}^B = s_{ij}^B(\varepsilon_{ij}^r|_t + \Delta \varepsilon_{ij}^r)$. The non-linear equations in Eq. (A.3) are solved with a Newton–Raphson method. Therefore, the derivatives of the functions f_{ij} with respect to $\Delta \varepsilon_{ij}^r$ are required. These can be written as

$$\frac{\partial f_{ij}}{\partial \Delta \varepsilon_{kl}^r} = \frac{\sigma_0}{\Delta \varepsilon^r} \delta_{ik} \delta_{jl} - \frac{2}{3} \frac{\sigma_0}{\Delta \varepsilon^r} \frac{\Delta \varepsilon_{ij}^r \Delta \varepsilon_{kl}^r}{(\Delta \varepsilon^r)^2} + \frac{3}{2} \left[2\mu \left(\delta_{ik} \delta_{jl} - \frac{1}{3} \delta_{ij} \delta_{kl} \right) + H_{ijkl} \right], \quad (\text{A.4})$$

where δ_{ij} is the Kronecker delta and H_{ijkl} are the components of the hardening tensor derived from the remanent potential Ψ^r as

$$H_{ijkl} = \frac{\partial^2 \Psi^r}{\partial \varepsilon_{ij}^r \partial \varepsilon_{kl}^r}. \quad (\text{A.5})$$

Note that Eq. (A.4) could only be written as such because the hardening tensor has the property that $H_{nnkl} = 0$ (summation is implied over n) due to the choice of invariants used to describe Ψ^r .

Even with this integration method, convergence was dependent on the strain increment size. Hence, for integration stations near the crack tip, the integration was broken into multiple steps, such that the strain increment was kept small enough to ensure convergence to the appropriate solution.

References

- Budiansky, B., Hutchinson, J.W., Lambropoulos, J.C., 1983. Continuum theory of dilatant transformation toughening in ceramics. *Int. J. Solids Struct.* 19, 337–355.
- Cocks, A.C.F., McMeeking, R.M., 1999. A phenomenological constitutive law for the behavior of ferroelectrics. *Ferroelectrics* 228, 219–228.
- Dean, R.H., Hutchinson, J.W., 1980. Quasi-static steady crack growth in small scale yielding. In: *Fracture Mechanics*, ASTM-STP 700, pp. 383–405.
- Fang, D., Li, C., 1999. Nonlinear electric-mechanical behavior of a soft PZT-51 ferroelectric ceramic. *J. Mater. Sci.* 34, 4001–4010.

- Fett, T., Thun, G., 1998. Nonsymmetric deformation behavior of lead zirconate titanate determined in bending tests. *J. Am. Ceram. Soc.* 81, 269–272.
- Fett, T., Müller, S., Munz, D., Thun, G., 1998. Nonsymmetry in the deformation behavior of PZT. *J. Mater. Sci. Lett.* 17, 261–265.
- Freund, L.B., Hutchinson, J.W., 1985. High strain-rate crack growth in rate-dependent plastic solids. *J. Mech. Phys. Solids* 33, 169–191.
- Frölich, A., 2001. Mikromechanisches modell zur ermittlung effektiver materialeigenschaften von piezoelektrischen polykristallen. Dissertation Thesis, Universität Karlsruhe, Germany.
- Huber, J.E., Fleck, N.A., Landis, C.M., McMeeking, R.M., 1999. A constitutive model for ferroelectric polycrystals. *J. Mech. Phys. Solids* 47, 1663–1697.
- Hutchinson, J.W., 1974. On steady quasi-static crack growth. Harvard University Report, Division of Applied Sciences, DEAP S-8.
- Hutchinson, J.W., 1979. A course on nonlinear fracture mechanics. Department of Solid Mechanics, Technical University of Denmark.
- Kamlah, M., 2001. Ferroelectric and ferroelastic piezoceramics—modeling and electromechanical hysteresis phenomena. *Continuum Mech. Thermodyn.* 13, 219–268.
- Kreher, W., 2002. Influence of domain switching zones on the fracture toughness of ferroelectrics. *J. Mech. Phys. Solids* 50, 1029–1050.
- Landis, C.M., 2002a. Fully coupled, multi-axial, symmetric constitutive laws for polycrystalline ferroelectric ceramics. *J. Mech. Phys. Solids* 50, 127–152.
- Landis, C.M., 2002b. Uncoupled, asymptotic mode III and mode E crack tip solutions in non-linear ferroelectric materials. *Eng. Fract. Mech.* 69, 13–23.
- Landis, C.M., 2003. On the strain saturation conditions in polycrystalline ferroelastic ceramics. *J. Appl. Mech.*, in press.
- Landis, C.M., Pardoën, T., Hutchinson, J.W., 2000. Crack velocity dependent toughness in rate dependent materials. *Mech. Mater.* 32, 663–678.
- Lucato, S.L., Lupascu, D.C., Rödel, J., 2000. Effect of poling direction on R-curve behavior in lead zirconate titanate. *J. Am. Ceram. Soc.* 83, 424–426.
- Lynch, C.S., 1996. The effect of uniaxial stress on the electro-mechanical response of 8/65/35 PLZT. *Acta Mater.* 44, 4137–4148.
- McMeeking, R.M., Evans, A.G., 1982. Mechanics of transformation toughening in brittle materials. *J. Am. Ceram. Soc.* 65, 242–246.
- Meschke, F., Raddatz, O., Kolleck, A., Schneider, G.A., 2000. R-curve behavior and crack-closure stresses in barium titanate and (Mg,Y)-PSZ ceramics. *J. Am. Ceram. Soc.* 83, 353–361.
- Oates, W.S., Lynch, C.S., Rödel, J., Lupascu, D., Aulbach, E., 2003. Investigation of subcritical crack growth in lead zirconate titanate. *J. Am. Ceram. Soc.*, submitted for publication.
- Ponte Castañeda, P., 1987. Asymptotic fields in steady crack growth with linear strain-hardening. *J. Mech. Phys. Solids* 35, 227–268.
- Reece, M.J., Guiu, F., 2002. Toughening produced by crack-tip-stress-induced domain reorientation in ferroelectric and/or ferroelastic materials. *Philos. Mag. A* 82, 29–38.
- Rice, J.R., 1968. A path independent integral and the approximate analysis of strain concentration by notches and cracks. *J. Appl. Mech.* 35, 379–386.
- Rice, J.R., 1972. Some remarks on elastic crack-tip stress fields. *Int. J. Solids Struct.* 8, 751–758.
- Schäufele, A.B., Härdtl, K.H., 1996. Ferroelastic properties of lead zirconate titanate ceramics. *J. Am. Ceram. Soc.* 79, 2637–2640.
- Yang, W., Zhu, T., 1998. Switch toughening of ferroelectrics subjected to electric fields. *J. Mech. Phys. Solids* 46, 291–311.
- Zhu, T., Yang, W., 1997. Toughness variation of ferroelectrics by polarization switch under non-uniform electric field. *Acta Mater.* 45, 4659–4702.

Erratum

Erratum to “On the fracture toughness of
ferroelastic materials”

J. Mech. Phys. Solids 51 (2003) 1347–1369[☆]

Chad M. Landis*

Department of Mechanical Engineering and materials Science, MS 321, Rice University,
P.O. Box 1892, Houston, TX 77251, USA

With regret, Fig. 6 in the original article was originally published with errors. The corrected version is shown below:

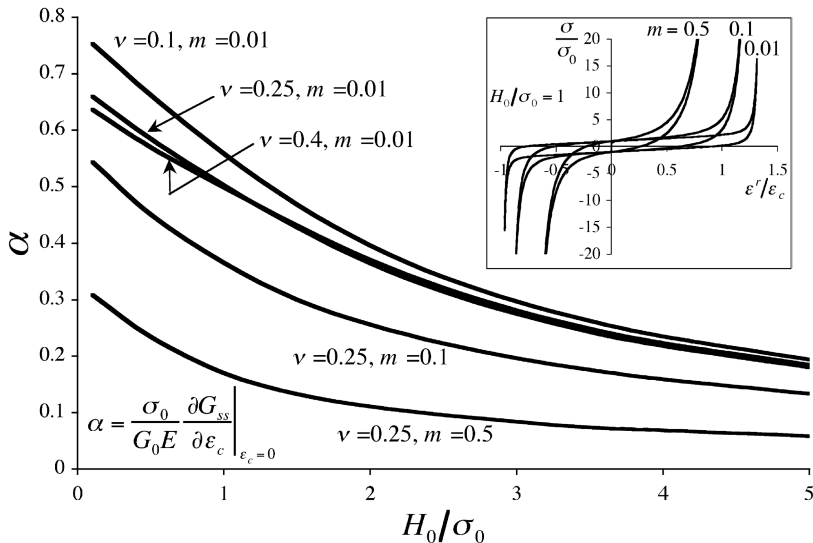


Fig. 6. The initial slope of the toughness ratio versus the relative saturation strain, as a function of the initial hardening H_0/σ_0 , for a range of Poisson’s ratio and m . The inset plots hysteresis loops in order to illustrate the dependence of the stress–strain behavior on m .

[☆] doi of original article S0022-5096(03)00065-6.

* Tel.: +1-713-348-3609; fax: +1-713-348-5423.

E-mail address: landis@rice.edu (C.M. Landis).

On page 1356, in Figure 3, the contours labeled as $\varepsilon_e^r = 0, \dots, 5$ should be labeled as *normalized* effective strain, i.e. $\varepsilon_e^r E / \sigma_0 = 0, \dots, 5$.

On page 1368, the first radicand in Equation A.2 should be changed such that the first line of the equation reads

$$\Delta \varepsilon^r = \sqrt{\frac{2}{3}} \Delta \varepsilon_{ij}^r \Delta \varepsilon_{ij}^r = \lambda \sqrt{\frac{2}{3}} (s_{ij} - s_{ij}^B)(s_{ij} - s_{ij}^B) = \frac{2}{3} \sigma_0 \lambda.$$